Multiple flow transitions in a box heated from the side in low-Prandtl-number fluids

D. Henry and H. BenHadid
Laboratoire de Mécanique des Fluides et d'Acoustique, CNRS/Université de Lyon, Ecole Centrale de Lyon/Université Lyon 1/INSA de Lyon, ECL, 36 avenue Guy de Collongue, 69134 Ecully Cedex, France
(Received 24 July 2006; revised manuscript received 1 June 2007; published 27 July 2007)

The determination of the flow transitions in a cavity heated from the side in low-Prandtl-number fluids has been a challenge for many years. Contrarily to the Rayleigh-Bénard situation, these transitions occur in already very intense convective flows, and the problem has been up to now mainly treated in two-dimensional situations. Thanks to a performing numerical method, the thresholds corresponding to the first flow transition in a three-dimensional (3D) parallelepipedic cavity have been determined for a wide range of aspect ratios and Prandtl number values. We obtain a kind of map of the transitions involved. Such a map of transitions is quite usual for Rayleigh-Bénard or Marangoni-Bénard situations, but completely new for 3D cavities heated from the side. The most striking result is the very frequent change of stability branches when the aspect ratios or Prandtl number are changed, which indicates different flow structures triggered at the thresholds, either steady or oscillatory, and breaking some of the symmetries of the problem.

DOI: 10.1103/PhysRevE.76.016314 PACS number(s): 47.20.Bp

I. INTRODUCTION

Sidewall convection is a heat and mass transfer problem of significance in both fundamental fluid mechanics and engineering applications such as crystal growth [1]. In the case of the flow in a parallelepipedic cavity, the basic flow is a simple unicellular circulation. When the horizontal temperature gradient is increased, however, the flow becomes more complex, undergoes bifurcations, and becomes unsteady and eventually turbulence sets in for large temperature differences.

Our interest is in the first onset of the time dependence in such convective flows, with relevance to metallic or semiconductor materials processing. In practical flows, instabilities in the melt phase during crystal growth can be frozen into the solid product and degrade the performance of semiconductor devices [2]. The melts are good thermal conductors, so that the Prandtl number Pr (the ratio of the viscous to the thermal diffusivity) is small. This will support our choice of small values of Pr ranging from 0 to 0.03. The other important parameters of these situations are the aspect ratios of the cavity (relative dimensions scaled by the dimensional height) and the Grashof number Gr proportional to the applied temperature difference.

The transition to unsteady convection in low-Prandtl-number fluids inside rectangular cavities has been experimentally studied since the first work of Hurle *et al.* [3] in 1974. These studies concern large- [4,5] or moderate- [3,6–12] aspect-ratio cavities containing mercury (Pr ≈ 0.026) or gallium (Pr ≈ 0.019). Typical temperature differences are 2.24 K for a 3.2 cm $\times$ 1.6 cm $\times$ 1 cm cavity [8] and 12 K for a 5 cm $\times$ 1.3 cm $\times$ 1 cm cavity [12]; some non-Boussinesq effects due to thermal conductivity and dynamic viscosity variations along the length of the cavity are reported in the second case, but they only affect the details of the transition [12]. These studies generally give oscillatory thresholds and temperature time series, and report the influence of either the aspect ratios, the Prandtl number, or an externally applied magnetic field. The results obtained are often difficult to analyze because of a lack of flow visualizations due to the opacity of the fluids involved, so that the need for theoretical and numerical investigations is essential.

Theoretical or numerical predictions of the unsteady transition in such cavities have also been reported, first for the one-dimensional parallel flow in an infinitely extended layer [13–15], then for the flow in two-dimensional cavities. The difficulties raised in solving such a problem have led to the organization of a GAMM workshop [16] where a numerical benchmark problem was proposed. These predictions, although interesting, are in fact of limited relevance for the realistic confined cavities of interest here. Finally, the three-dimensional numerical studies are few, because the flows and the transitions are complex, which necessitates fine meshes and high-performance numerical methods. Such studies are focused on specific aspect ratios [17,18] or do not detail the different transitions encountered when changing the aspect ratios or the Prandtl number [19].

Our study concerns convection in a three-dimensional parallelepipedic cavity and is focused on the determination of the thresholds corresponding to the first flow transition for a wide range of aspect ratios and Prandtl number values. We are able to discriminate the different transitions which occur. They appear as different branches of stability thresholds corresponding to different flow structures triggered at the thresholds.

II. MATHEMATICAL MODEL AND NUMERICAL TECHNIQUES

A. Mathematical model

The mathematical model consists of a rectangular parallelepiped cavity filled with low-Pr fluids and heated from the side. The cavity has aspect ratios $A_x = L/h$ and $A_y = l/h$, where L is the length of the cavity (along x), h is its height (along z), and l is its width (along y), as shown schematically in Fig. 1. The vertical end walls are isothermal and held at different temperatures $\bar{T}_h$ at the right, hot end wall and $\bar{T}_c$ at

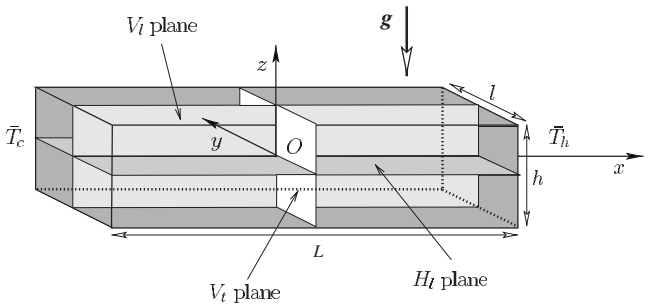

FIG. 1. Geometry of the differentially heated cavity.

the left, cold end wall, whereas the sidewalls are adiabatic. The fluid is assumed to be Newtonian with constant physical properties (kinematic viscosity ν, thermal diffusivity κ, density ρ), except that, according to the Boussinesq approximation, the fluid density is considered as temperature dependent in the buoyancy term with a linear law $\rho=\rho_m[1-\beta(\bar{T}-\bar{T}_m)]$, where β is the thermal expansion coefficient and $\bar{T}_m$ a reference temperature taken as the mean temperature $(\bar{T}_h+\bar{T}_c)/2$. The convective motions are then modeled by the Navier-Stokes equations coupled to an energy equation. Using h, h^2/ν, ν/h, $\rho\nu^2/h^2$, and $\gamma=(\bar{T}_h-\bar{T}_c)/A_x$ as scales for length, time, velocity, pressure, and temperature, respectively, these equations take the following form:

$$\nabla \cdot \boldsymbol{u} = 0, \tag{1}$$

$$\frac{\partial \boldsymbol{u}}{\partial t} + (\boldsymbol{u}\cdot\nabla)\boldsymbol{u} = -\nabla p + \nabla^2 \boldsymbol{u} + \mathrm{Gr} T \boldsymbol{e}_z, \tag{2}$$

$$\frac{\partial T}{\partial t} + (\boldsymbol{u}\cdot\nabla)T = \frac{1}{\mathrm{Pr}}\nabla^2 T, \tag{3}$$

with boundary conditions given by $\partial T/\partial z=0$ on $z=\pm 1/2$ and $\partial T/\partial y=0$ on $y=\pm A_y/2$, $T=-A_x/2$ on $x=-A_x/2$ and $T=A_x/2$ on $x=A_x/2$, and $\boldsymbol{u}=0$ on all boundaries. The dimensionless variables are the velocity vector $\boldsymbol{u}=(u,v,w)$, the pressure p, and the temperature $T=(\bar{T}-\bar{T}_m)/\gamma$, $\boldsymbol{e}_z$ is the unit vector in the vertical direction, and the nondimensional parameters are the Grashof number $\mathrm{Gr}=\beta g \gamma h^3/\nu^2$ and the Prandtl number $\mathrm{Pr}=\nu/\kappa$.

Under the approximation of the model, the steady convective flows obtained at moderate Gr in such cavity [18] present different symmetries: a reflection symmetry S_l with respect to the longitudinal V_l plane (left-right symmetry) and a π-rotational symmetry S_r about the transverse y axis. These symmetries are defined, respectively, as

$$S_l: \quad (x,y,z,t) \to (x,-y,z,t), \quad (u,v,w,T) \to (u,-v,w,T), \tag{4}$$

$$S_r: \quad (x,y,z,t) \to (-x,y,-z,t),$$

$$(u,v,w,T) \to (-u,v,-w,-T). \tag{5}$$

The combination of these two symmetries gives a symmetry S_c with respect to the center point of the cavity ($S_c=S_l\cdot S_r$). When increasing Gr, bifurcations to new flow states (steady or oscillatory) will occur, at which some of these symmetries will usually be broken.

B. Numerical techniques

The governing equations of the model were solved in the three-dimensional domain using a spectral element method, as described in [20]. The spatial discretization is obtained through Gauss-Lobatto-Legendre points distributions; the time discretization is carried out using a semi-implicit splitting scheme where, as proposed by Karniadakis *et al.* [21], the nonlinear terms are first integrated explicitly, the pressure is then solved through a pressure equation enforcing the incompressibility constraint (with a consistent pressure boundary condition derived from the equations of motion), and the linear terms are finally integrated implicitly. This time integration scheme is used for transient computations with the third-order accurate formulation described in [21]. But in its first-order formulation, it is also used for steady state solving [22] and calculation of bifurcation points [23,24] through a Newton method. These methods which are essential for our study are succinctly described in the following.

The first-order time scheme can be written in the abbreviated form

$$\frac{\boldsymbol{X}^{(n+1)}-\boldsymbol{X}^{(n)}}{\Delta t} = \mathcal{N}(\boldsymbol{X}^{(n)},\mathrm{Gr}) + \mathcal{L}\boldsymbol{X}^{(n+1)}. \tag{6}$$

Here, $\boldsymbol{X}$ represents all of the spatially discretized fields $(\boldsymbol{u}(u,v,w),T)$, and $\mathcal{N}$ and $\mathcal{L}$ represent the spatially discretized nonlinear and linear operators. We can also consider a slightly modified scheme which is expressed as

$$\frac{\boldsymbol{X}^{(n)}-\boldsymbol{X}^{(n)}}{\Delta t} = \mathcal{N}(\boldsymbol{X}^{(n)},\mathrm{Gr}) + \mathcal{L}\boldsymbol{X}^{(n+1)} \tag{7}$$

or, after some algebra, can be rewritten as

$$\boldsymbol{X}^{(n+1)}-\boldsymbol{X}^{(n)} = -\mathcal{L}^{-1}[\mathcal{N}(\boldsymbol{X}^{(n)},\mathrm{Gr}) + \mathcal{L}\boldsymbol{X}^{(n)}]. \tag{8}$$

Now we consider the steady-state problem

$$0 = \mathcal{N}(\boldsymbol{X},\mathrm{Gr}) + \mathcal{L}\boldsymbol{X}. \tag{9}$$

To use Newton's method on Eq. (9), at each step we must solve

$$[\mathcal{N}_{\boldsymbol{X}}(\boldsymbol{X},\mathrm{Gr}) + \mathcal{L}]\delta\boldsymbol{X} = -[\mathcal{N}(\boldsymbol{X},\mathrm{Gr}) + \mathcal{L}\boldsymbol{X}],$$

$$\boldsymbol{X} \leftarrow \boldsymbol{X} + \delta\boldsymbol{X}, \tag{10}$$

where $\mathcal{N}_{\boldsymbol{X}}(\boldsymbol{X},\mathrm{Gr})$ is the Jacobian of $\mathcal{N}$ with respect to $\boldsymbol{X}$ evaluated at $\boldsymbol{X}$ and Gr. Instead of solving (10), we solve

$$-\mathcal{L}^{-1}[\mathcal{N}_{\boldsymbol{X}}(\boldsymbol{X},\mathrm{Gr}) + \mathcal{L}]\delta\boldsymbol{X} = -(-\mathcal{L}^{-1})[\mathcal{N}(\boldsymbol{X},\mathrm{Gr}) + \mathcal{L}\boldsymbol{X}]. \tag{11}$$

The operator $-\mathcal{L}^{-1}$ serves as a preconditioner (i.e., approximate inverse) for $\mathcal{N}+\mathcal{L}$, greatly accelerating iterative inversion.

If we solve the linear system (11) by an iterative conjugate gradient method, we need only provide the right-hand

side and the action of the matrix-vector product constituting the left-hand side. Referring to Eq. (8), we see that the right-hand side of Eq. (11) can be obtained by carrying out the adapted time step and the matrix-vector product by carrying out a linearized version of the same time step. We emphasize that the Jacobian matrix is never constructed or stored. The GMRES algorithm from the NSPCG software library [25] is used as iterative solver.

The direct calculation of bifurcation points is more complex but follows the same ideas. We give the case of the steady bifurcation point as an example. At such a point, $\boldsymbol{X}$ is a solution to Eq. (9) and the Jacobian is singular, with a null vector $\boldsymbol{h}$ whose lth component will be normalized to 1:

$$\mathcal{N}(\boldsymbol{X},\mathrm{Gr}) + \mathcal{L}\boldsymbol{X} = 0, \tag{12}$$

$$[\mathcal{N}_{\boldsymbol{X}}(\boldsymbol{X},\mathrm{Gr}) + \mathcal{L}]\boldsymbol{h} = 0, \tag{13}$$

$$\boldsymbol{h}_l - 1 = 0. \tag{14}$$

One Newton step for solving Eqs. (12)–(14) is

$$\begin{bmatrix} \mathcal{N}_{\boldsymbol{X}}(\boldsymbol{X},\mathrm{Gr}) + \mathcal{L} & 0 & \mathcal{N}_{\mathrm{Gr}}(\boldsymbol{X},\mathrm{Gr}) \\ \mathcal{N}_{\boldsymbol{X},\boldsymbol{X}}(\boldsymbol{X},\mathrm{Gr})\boldsymbol{h} & \mathcal{N}_{\boldsymbol{X}}(\boldsymbol{X},\mathrm{Gr}) + \mathcal{L} & \mathcal{N}_{\boldsymbol{X},\mathrm{Gr}}(\boldsymbol{X},\mathrm{Gr})\boldsymbol{h} \\ 0 & e_l^T & 0 \end{bmatrix} \begin{bmatrix} \delta\boldsymbol{X} \\ \delta\boldsymbol{h} \\ \delta\mathrm{Gr} \end{bmatrix} = - \begin{bmatrix} \mathcal{N}(\boldsymbol{X},\mathrm{Gr}) + \mathcal{L}\boldsymbol{X} \\ [\mathcal{N}_{\boldsymbol{X}}(\boldsymbol{X},\mathrm{Gr}) + \mathcal{L}]\boldsymbol{h} \\ 0 \end{bmatrix},$$

$$\boldsymbol{X} \leftarrow \boldsymbol{X} + \delta\boldsymbol{X},$$

$$\boldsymbol{h} \leftarrow \boldsymbol{h} + \delta\boldsymbol{h},$$

$$\mathrm{Gr} \leftarrow \mathrm{Gr} + \delta\mathrm{Gr}. \tag{15}$$

In this system, $\mathcal{N}_{\mathrm{Gr}}$ is the Jacobian of $\mathcal{N}$ with respect to Gr, $\mathcal{N}_{\boldsymbol{X},\boldsymbol{X}}$ is the double Jacobian of $\mathcal{N}$ with respect to $\boldsymbol{X}$, $\mathcal{N}_{\boldsymbol{X},\mathrm{Gr}}$ is the Jacobian of $\mathcal{N}$ with respect to both $\boldsymbol{X}$ and Gr, and e_l^T is the transpose of the lth unit vector. Preconditionned as Eq. (11), this system can still be solved by conjugate gradient iterations. As before, the different terms of the right-hand side and of the matrix-vector product are obtained by minor modifications of the first-order time integration scheme. (See, for example, [24] for more details.)

Finally, in order to initiate the calculation of bifurcation points, we have to calculate leading eigenvalues—those with largest real part and thus responsible for initiating instability—and their corresponding eigenvectors. To do so, we use Arnoldi's method from the ARPACK library. As described in [22], by time stepping the linearized equations of the problem [linearized version of Eq. (6)] with a small time step, we are able to calculate the exponential of the leading eigenvalues through the Arnoldi method with good accuracy. In this way, with a time step equal to 10^{-5}, we have computed the ten first real or complex leading eigenvalues and their corresponding eigenvectors.

TABLE I. Mesh refinement tests of numerical accuracy of the critical Grashof number corresponding to the first steady transition for $A_x=4$, $A_y=6$, and Pr=0.01.

Mesh	$39\times41\times19$	$43\times45\times23$	$47\times49\times27$	$51\times53\times31$
Gr_c	20435.537	20431.687	20431.652	20431.526

III. RESULTS

Our results concern various cavities ranging from $A_x=2$ to $A_x=5$ and from $A_y=1$ to $A_y=6$. For all these cavities, the same refined mesh comprising $47\times49\times27$ points (in the x, y, and z directions, respectively) was chosen. It gives a very good precision for the threshold calculations in any case (see the precision tests given in Table I for $A_x=4$, $A_y=6$).

We have focused our study on the precise determination of the instability thresholds with characterization of the types of instabilities involved when changing both aspect ratios and the Prandtl number. More precisely, for Pr=0.01 we have first changed the longitudinal aspect ratio A_x from 2 to 5 for a cavity with a large transverse extension ($A_y=6$). For the same value of Pr and $A_x=4$, we have widely changed the transverse confinement with A_y varying from 6 to 1. Finally, the effect of the Prandtl number ($10^{-7}\leqslant\mathrm{Pr}\leqslant0.03$) has been studied for the cavity $A_x=4$, $A_y=2$ already considered by Henry and Buffat [18]. The step used for changing both aspect ratios is 0.1, whereas it is 0.001 for Pr. A preliminary calculation of the ten leading eigenvalues and eigenvectors for the same aspect ratios and Prandtl numbers has guided our threshold calculations and allowed us to obtain clear and sound results.

A. Instability thresholds

The instability thresholds are first given as a function of A_x in Fig. 2(a). In this figure as in the other figures giving thresholds, different symbols have been used to characterize the symmetries of the eigenvector involved in the corresponding transition. More precisely, squares have been used to indicate eigenvectors with the S_l (left-right) symmetry (S_l modes), circles for eigenvectors with only the S_c (center) symmetry (S_c modes), triangles for eigenvectors with the S_r (π-rotational) symmetry (S_r modes), and crosses for eigenvectors having kept all the symmetries (which we will call the S symmetries and the corresponding modes S modes). Moreover the curves are plotted with a solid line for the steady transitions and with a dashed line for the oscillatory transitions.

For a cavity with a large transverse extension ($A_y=6$), varying A_x from 2 to 5 leads to great changes in the threshold values and in the type of instability involved at the transition [Fig. 2(a)]. The thresholds increase from 13 897 for $A_x=5$ to 39 931 for $A_x=2$, showing a clear stabilization of the convection by the confinement in the x direction. For $A_x=5$, despite a slower variation of the thresholds, we have still not reached a clear asymptotic value which would be characteristic of long cavities. The more striking observation is the frequent change of instability mode when A_x is modified. For A_x be-

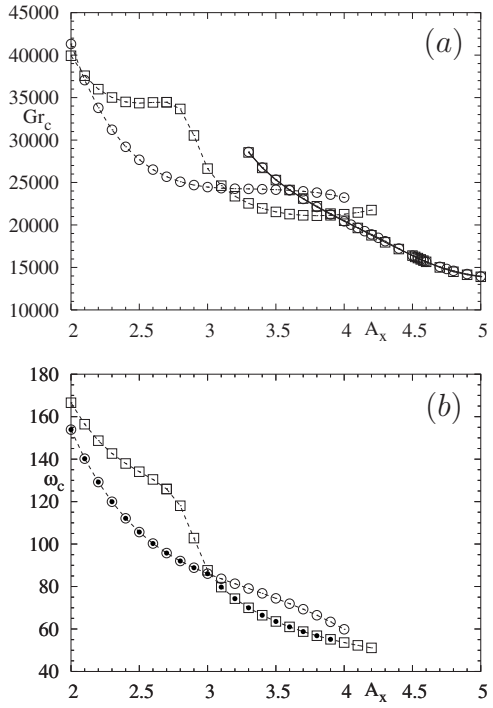

FIG. 2. Instability thresholds (a) and angular frequencies of the oscillatory modes (b) for $2 \leqslant A_x \leqslant 5$ ($A_y=6$ and Pr=0.01). Solid curves represent steady transitions and dashed curves oscillatory transitions. Circles indicate S_c modes at the transition and squares S_l modes. The black dots in (b) indicate the critical angular frequencies.

tween 2 and 3.9, the instability is oscillatory, triggered by an S_l mode (keeping the left-right symmetry) for $A_x=2$ and for $3.2 \leqslant A_x \leqslant 3.9$ and by an S_c mode (keeping the central symmetry) for $2.1 \leqslant A_x \leqslant 3.1$. Beyond $A_x=4$, the instability is stationary, with two modes which are very close to one another and become successively the critical mode, as is shown more clearly in Fig. 3 where both thresholds are plotted relatively to their mean value. Considering the range of A_x where the steady modes are the critical modes ($A_x \geqslant 4$), it is observed that the S_c mode is dominant for $A_x=4$ and for $4.5 \leqslant A_x$

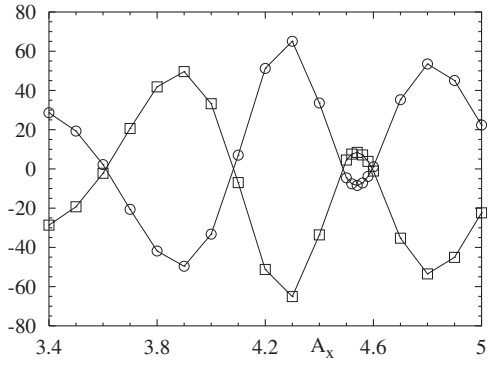

FIG. 3. Precisions on the variation of the instability thresholds for the steady transitions for $3.4 \leqslant A_x \leqslant 5$. The variation of both thresholds is given around their arithmetic mean value ($A_y=6$ and Pr=0.01). Circles indicate S_c modes at the transition and squares S_l modes.

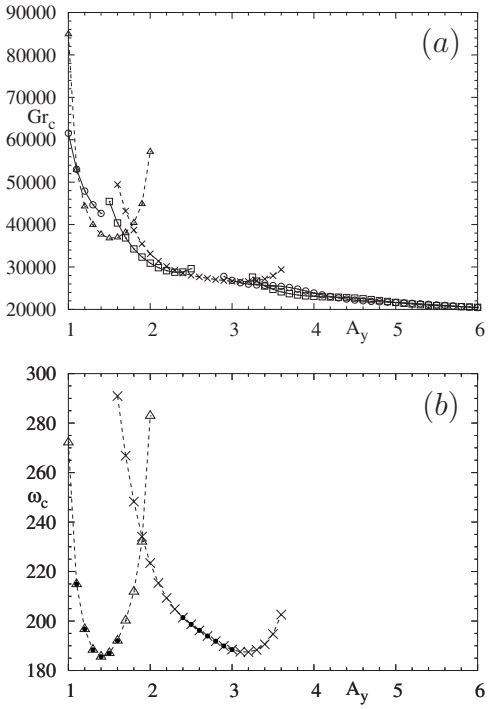

FIG. 4. Instability thresholds (a) and angular frequencies of the oscillatory modes (b) for $1 \leqslant A_y \leqslant 6$ ($A_x=4$ and Pr=0.01). Solid curves represent steady transitions and dashed curves oscillatory transitions. Circles indicate S_c modes at the transition, squares S_l modes, triangles S_r modes, and crosses S modes. The black dots in (b) indicate the critical angular frequencies.

< 4.6 and that the S_l mode is dominant for $4.1 \leqslant A_x < 4.5$ and for $4.6 \leqslant A_x \leqslant 5$. Moreover, the maximum difference in Gr between the two modes is found to be less than 140. Finally, concerning the angular frequencies of the oscillatory modes [Fig. 2(b)], they globally decrease as the thresholds decrease with increasing A_x, going from values around 160 for $A_x=2$ to values close to 50 for A_x around 4.

Still for Pr=0.01, the longitudinal aspect ratio is now fixed to $A_x=4$ and the transverse extension is decreased from $A_y=6$ to $A_y=1$. The corresponding instability thresholds are given as a function of A_y in Fig. 4(a). We see that the thresholds globally increase when the transverse extension is decreased (increase of the confinement), with a rather slow and quite regular increase for A_y between 6 and 2 and a stronger increase below $A_y=2$ becoming very steep around $A_y=1$. The types of transitions involved are here also numerous, which gives nonsmooth threshold curves. A steady transition is found to occur in a wide range of values of A_y, for $3 < A_y \leqslant 6$, around $A_y=2$, and also for $A_y=1$. As previously when A_x was changed, this steady transition corresponds either to an S_c mode or to an S_l mode. As can be seen more precisely in Fig. 5, the two modes are alternatively critical for $3 < A_y \leqslant 6$ [Fig. 5(b)], whereas the S_l mode is critical for $1.7 \leqslant A_y \leqslant 2.3$ [Fig. 5(a)] and the S_c mode for $A_y=1$.

Oscillatory transitions are also found for $2.4 \leqslant A_y \leqslant 3$ and for $1.1 \leqslant A_y \leqslant 1.6$, but they correspond to two other modes [Fig. 5(a)]. In the first range of A_y, the oscillatory transition occurs without loss of symmetry (S mode), whereas in the second range it corresponds to a mode only keeping the

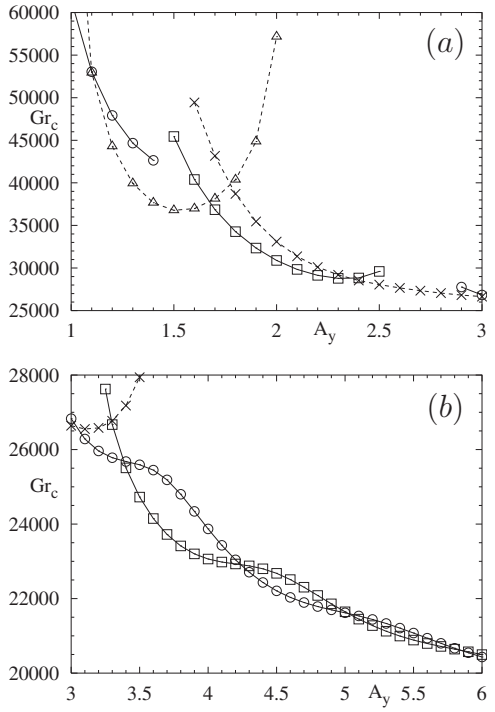

FIG. 5. Precisions on the variation of the instability thresholds for $1 \leqslant A_y \leqslant 3$ (a) and for $3 \leqslant A_y \leqslant 6$ (b) ($A_x=4$ and Pr=0.01). Solid curves represent steady transitions and dashed curves oscillatory transitions. Circles indicate S_c modes at the transition, squares S_l modes, triangles S_r modes, and crosses S modes.

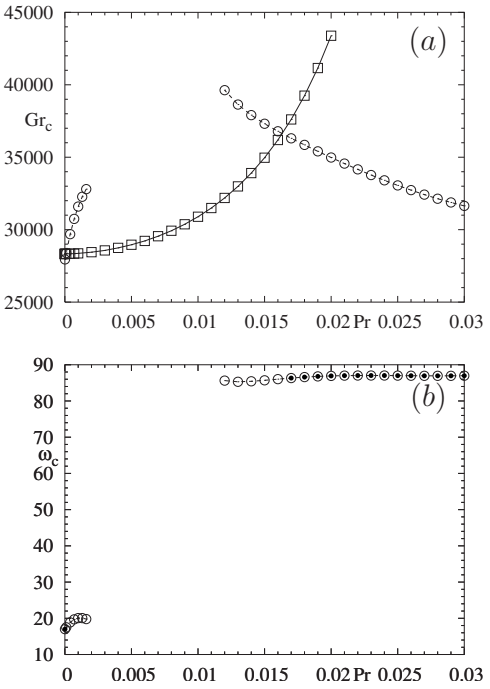

FIG. 6. Instability thresholds (a) and angular frequencies of the oscillatory modes (b) for $0.00001 \leqslant \mathrm{Pr} \leqslant 0.03$ ($A_x=4$ and $A_y=2$). Solid curves represent steady transitions and dashed curves oscillatory transitions. Circles indicate S_c modes at the transition and squares S_l modes. The black dots in (b) indicate the critical angular frequencies.

π-rotational symmetry about the y axis (S_r mode). Concerning the angular frequencies of these oscillatory modes [Fig. 4(b)], they follow the variation of the thresholds for each mode. If we now only consider the critical values of angular frequency, when A_y is decreased, they are found to slowly increase from 188 to 202 for the S modes and to vary from 192 down to 185 and then more steeply up to 215 for the S_r modes. Finally, considering the global variation of the thresholds [Fig. 4(a)], we see that, despite a slower decrease of the thresholds when A_y is increased, even for $A_y=6$ (quite large transverse extension) a clear asymptotic value, which would be characteristic of pure two-dimensional situations independent of this transverse extension, has not been reached.

Finally, the effect of the Prandtl number ($10^{-7} \leqslant \mathrm{Pr} \leqslant 0.03$) is studied for the cavity with aspect ratios $A_x=4$ and $A_y=2$. The corresponding instability thresholds are given as a function of Pr in Fig. 6(a). We see that for $A_x=4$ and $A_y=2$, the first transition is a steady transition in a wide range of Pr values between 0.0001 and 0.016. This steady transition corresponds to an S_l mode and the corresponding thresholds increase when Pr is increased. For larger values of Pr ($0.017 \leqslant \mathrm{Pr} \leqslant 0.03$), the first transition is oscillatory with angular frequencies around 87 [Fig. 6(b)] and corresponds to an S_c mode only keeping the symmetry with respect to the center of the cavity, in agreement with the results found by Henry and Buffat [18] for the same cavity and Pr=0.026, results which were favorably compared with the experimental data given in [4,7,8]. In [18], the authors also found a similar oscillatory transition but with a much smaller frequency, for the limit case Pr=0. We confirm this result, as we find an oscillatory transition corresponding to an S_c mode with an angular frequency close to 17 for very small values of Pr. But our results also show that this oscillatory transition obtained at Pr=0 is in fact critical only for very weak values of Pr, more precisely for $\mathrm{Pr} < 0.0001$ (Fig. 7). For such a cavity, contrarily to what could be expected or at least hoped, the transition observed at Pr=0 is then not at all characteristic of the transitions which occur in the whole range of weak values of Pr corresponding to liquid metals.

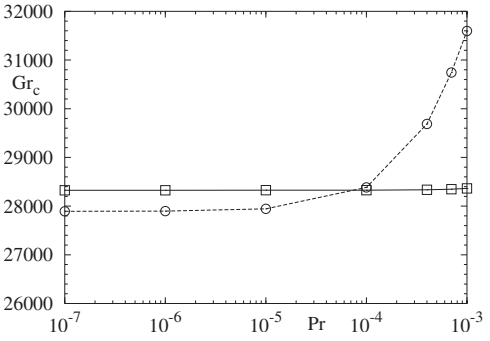

FIG. 7. Precisions on the variation of the instability thresholds for Pr close to 0 ($A_x=4$ and $A_y=2$). Solid curves represent steady transitions and dashed curves oscillatory transitions. Circles indicate S_c modes at the transition and squares S_l modes.

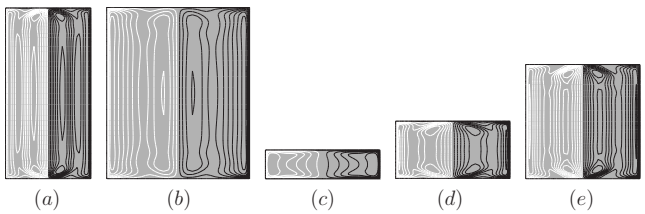

FIG. 8. Basic steady flows at the critical thresholds: isovalues of the vertical velocity in the H_l plane (black and white lines for positive and negative isovalues, respectively). (a) $A_x=3$, $A_y=6$, (b) $A_x=5$, $A_y=6$, (c) $A_x=4$, $A_y=1$, (d) $A_x=4$, $A_y=2$, and (e) $A_x=4$, $A_y=4$. The view is from above and the direction x is horizontal in the pictures (Pr=0.01).

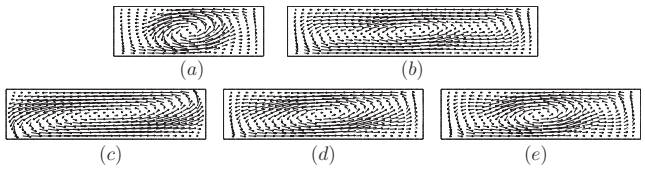

FIG. 9. Basic steady flows at the critical thresholds: velocity vectors in the V_l plane. (a) $A_x=3$, $A_y=6$, (b) $A_x=5$, $A_y=6$, (c) $A_x=4$, $A_y=1$, (d) $A_x=4$, $A_y=2$, and (e) $A_x=4$, $A_y=4$ (Pr=0.01).

B. Analysis of the flows

1. Basic flow states

The structure of the basic flows at the critical thresholds is illustrated in Figs. 8 and 9. Different aspect ratios covering our domain of study are chosen. Figure 8 displays the isovalues of the vertical velocity in the horizontal H_l plane and Fig. 9 the velocity vectors in the vertical V_l plane. The flow is found to be quite invariant in the transverse direction y (except close to the front and back boundaries) when the aspect ratio A_y is increased (Fig. 8). This invariance is however not perfect, even for the large boxes with $A_y=6$ [Figs. 8(a) and 8(b)], which may explain that an asymptotic value for the thresholds is still not reached when A_y is increased up to 6.

Another interesting feature depicted in Fig. 8 is that, except for $A_y=1$, two maxima and two minima are found for the vertical velocity in the H_l plane. This means that in these cases, the flow structure is no longer the simple unicellular circulation found at small Gr but rather corresponds to a centered roll-like structure inside the long-scale circulation. This roll-like structure is clearly visible in the V_l plane [Figs. 9(a), 9(b), 9(d), and 9(e)] and is particularly marked for $A_x=3$, $A_y=6$, and $A_x=4$, $A_y=4$ [Figs. 9(a) and 9(e)], two cases which are not much transversally confined and for which the thresholds are not too small. More details on the variation of the flow structure with the aspect ratios A_x and A_y can be obtained from the vertical velocity profiles along the longitudinal x axis given in Fig. 10. For $A_y=6$ and $2\leqslant A_x\leqslant 5$ [Fig. 10(a)], the positive and negative peaks of w located near the center of the cavity and corresponding to the roll-like structure are well pronounced. Two other peaks corresponding to the long-scale circulation are present close to the right and left end walls, except for $A_x=2$ (the shortest cavity) where the long-scale circulation is less distinguishable from the roll structure. For $A_x=4$ and $1\leqslant A_y\leqslant 6$ [Fig. 10(b)], the peaks corresponding to the long-scale circulation and those of the roll-like structure are well distinct, except for $A_y=1$ where the roll-like structure is not present. Moreover, the continuous variation of the profiles with A_y still indicates that no asymptotic behavior can be expected even up to $A_y=6$. Note that in spite of these evolutions, the basic flows keep the S symmetries which are characteristic of the steady flows at small Gr.

Such an evolution of the steady flows was already mentioned by Henry and Buffat [18] for a cavity with aspect ratios $A_x=4$ and $A_y=2$. The authors indicate that the appearance of the roll-like structure is the sign of an imperfect bifurcation which is connected to the steady transition towards transverse rolls found by stability analysis of the parallel flow in the infinitely extended side-heated cavity (Laure [14], Kuo and Korpela [15]). These stability analyses indicate that this steady transition occurs first up to Pr=0.033 for adiabatic boundaries (which includes all the cases treated in the present study) and that the thresholds are about $\mathrm{Gr}_c=7943$, 8077, and 8520 for Pr=0.001, 0.01, and 0.03, respectively.

Our results show that this imperfect bifurcation towards a roll-like structure affects most side-heated cavities in the low-Prandtl-number domain, except the highly transversally confined cavities (A_y around 1 or below) and perhaps the

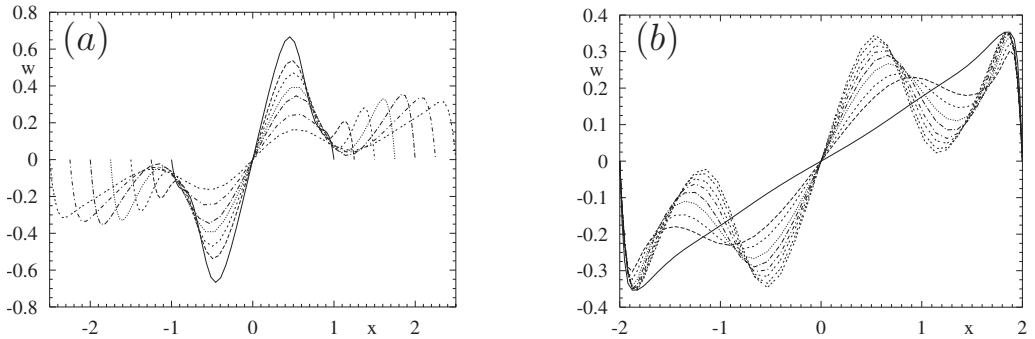

FIG. 10. Basic steady flows at the critical thresholds: vertical velocity profiles (scaled by $\sqrt{\mathrm{Gr}}\nu/h$) along the longitudinal x axis. (a) Profiles for $A_y=6$ and $A_x=2$, 2.5, 3, 3.5, 4, 4.5, and 5 (a solid curve is used for $A_x=2$, and the intensity of the peak close to the center decreases as A_x is increased). (b) Profiles for $A_x=4$ and $A_y=1$, 1.6, 2, 2.6, 3.2, 4, 4.6, 5.4, and 6 (a solid curve is used for $A_y=1$, and the intensity of the peak close to the center increases as A_y is increased) (Pr=0.01).

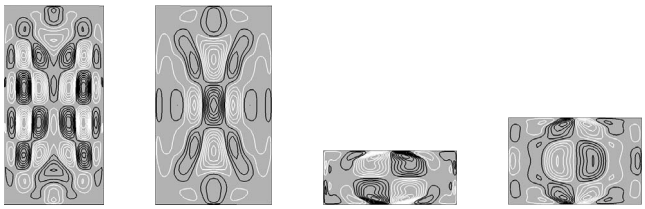

FIG. 11. Real part of the critical oscillatory modes: (a) with the S_c symmetry (A_x=3, A_y=6, Gr_c=24 456), (b) with the S_l symmetry (A_x=3.5, A_y=6, Gr_c=21 542), (c) with the S_r symmetry (A_x=4, A_y=1.6, Gr_c=36 974), and (d) with all the S symmetries (A_x=4, A_y=2.6, Gr_c=27 663). Isovalues of the vertical velocity in the H_l plane (black and white lines for positive and negative isovalues, respectively). The direction x is horizontal in the pictures (Pr =0.01).

very short cavities. The important consequence is that the transitions we have found in this paper for the three-dimensional cavities generally occur on a basic roll-like flow structure and not on a simple, almost parallel unicellular circulation, so that these transitions cannot be predicted by any parallel flow approximation. Finally, we can mention that the roll-like structure was not found by Hof *et al.* [12] for a transversally confined cavity with aspect ratios A_x=5 and A_y=1.3; this result is consistent with our observations.

2. Critical modes and symmetries

The symmetries have been shown to play an important role in the observed transitions in the three-dimensional laterally heated cavity. Indeed, these transitions break or not the different symmetries of the system, so that four modes with different symmetries (S symmetries, S_c symmetry, S_l symmetry, S_r symmetry) could be theoretically obtained. The calculations we performed for different values of A_x, A_y, and Pr allowed us to obtain these four types of modes for the oscillatory transitions and only the S_c and S_l modes for the steady transitions. The structure of these modes at their critical thresholds is shown in Fig. 11 in the case of oscillatory transitions by plots of the vertical velocity in the H_l plane. We recall that a mode (eigenvector) is symmetric with respect to some of the symmetries of the basic flow, but is also antisymmetric with respect to the other symmetries of the basic flow which are broken [18]. Moreover, according to (4) and (5), the vertical velocities have the same sign at points reflected about the V_l plane in the case of the S_l symmetry and opposite signs at points separated by a π rotation about the transverse y axis in the case of the S_r symmetry. This explains why for the S mode [no symmetry breaking, Fig. 11(d)] we find the changes of signs just described. For the S_c mode [breaking of both S_l and S_r symmetries, Fig. 11(a)] the changes of signs are opposite, i.e., the V_l plane separates opposite-sign zones and the y axis same-sign zones. For the S_l mode [breaking of the S_r symmetry, Fig. 11(b)] same-sign zones are found on both sides of the V_l plane and y axis, which gives a fully symmetric pattern in this case. Finally, for the S_r mode [breaking of the S_l symmetry, Fig. 11(c)] both the V_l plane and y axis delimit opposite-sign zones.

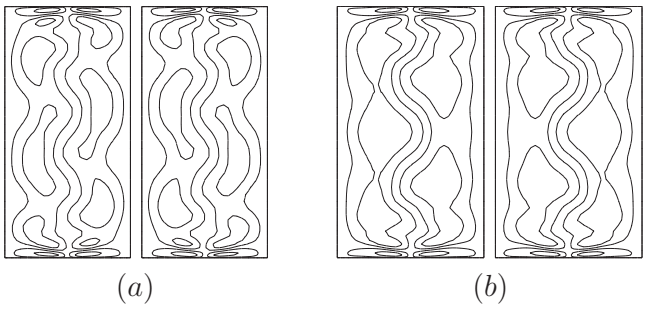

FIG. 12. Oscillatory flows obtained above the oscillatory critical thresholds: (a) with the S_c symmetry [Gr=25 000, A_x=3 (Gr_c =24 456)], (b) with the S_l symmetry [Gr=23 000, A_x=3.5 (Gr_c =21 542)]. Views of the longitudinal velocity (along x) in the H_l plane at 2 times half a period apart. The direction x is horizontal in the pictures (A_y=6, Pr=0.01).

These four types of modes will trigger different oscillatory flow structures beyond the thresholds. These structures are illustrated in Figs. 12 and 13 by oscillatory evolutions obtained close above the thresholds by time integration and plotted at 2 times half a period apart. As expected, these structures have the symmetries kept by the corresponding critical mode, and the time evolution gives specific spatial variations connected to these symmetries. Moreover, as was already indicated by Henry and Buffat [18], the broken symmetries are preserved between states separated by half a period [Figs. 12(a), 12(b), and 13(a)]. In the particular case shown in Fig. 13(b), there is no loss of symmetry and the states separated by half a period have no relation between them.

Finally, in the wide range of parameters where the first transition is steady, the oscillatory transition will only appear as a secondary instability on the steady solution branches which bifurcate from the basic branch at the steady transition point. As some of the original symmetries of the system are lost at the first steady transition, these secondary oscillatory instabilities will still be different from those already mentioned. As an example, we give the oscillatory flow obtained at Gr=24 000 for A_x=4, A_y=6, and Pr=0.01 in Fig. 14. In this case, the first steady transition only keeps the central symmetry, and the oscillatory transition which occurs at Gr_c=23336 on the steady bifurcated branches does not break any symmetries and then keeps this central symmetry.

C. Energy budgets at the transitions

It is interesting to know the physical mechanisms involved in these transitions. This information can be obtained

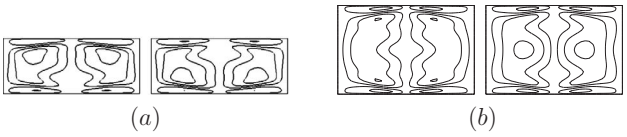

FIG. 13. Oscillatory flows obtained above the oscillatory critical thresholds: (a) with the S_r symmetry [Gr=38 000, A_y=1.6 (Gr_c =36 974)], (b) with all the S symmetries [Gr=28 000, A_y=2.6 (Gr_c=27 663)]. Views of the longitudinal velocity (along x) in the H_l plane at 2 times half a period apart. The direction x is horizontal in the pictures (A_x=4, Pr=0.01).

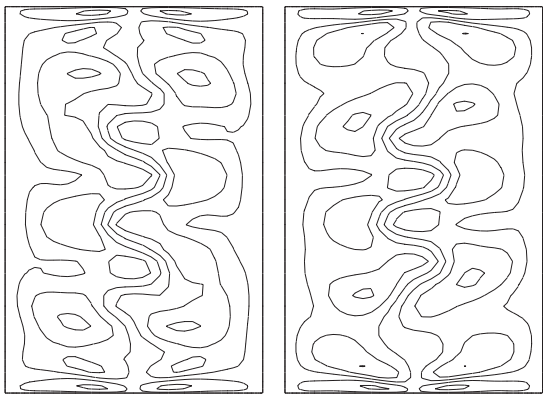

FIG. 14. Oscillatory flow obtained for Gr=24 000, A_x=4, A_y=6, and Pr=0.01. This flow is triggered at a Hopf bifurcation point (Gr_c=23 336) which appears on a secondary steady branch bifurcating from the steady basic branch at Gr_c=20 432. Views of the longitudinal velocity (along x) in the H_l plane at 2 times half a period apart. The direction x is horizontal in the pictures.

from the calculation at threshold of the fluctuating kinetic energy budget associated with the perturbations (critical eigenvector). The basic steady solution at threshold $[u,v,w,T](x,y,z)$ (or $[u_i,T](x_i)$) and the critical eigenvector $(u',v',w',T')(x,y,z)$ (or $[u_i',T'](x_i)$) both enter the equation of energy budget giving the rate of change of the fluctuating kinetic energy defined as $k=\mathrm{Re}(u_i'u_i'^*/2)$ (Re and the superscript $*$ denote the real part and the complex conjugate, respectively). After volume integration, an equation for the rate of change of the total fluctuating kinetic energy ($K=\int_\Omega k d\Omega$) can be written:

$$\frac{\partial K}{\partial t} = E_{shear} + E_{visc} + E_{buoy}, \tag{16}$$

where

$$E_{shear} = \mathrm{Re}\left(- \int_\Omega u_j' \frac{\partial u_i}{\partial x_j} u_i'^* d\Omega \right),$$

$$E_{visc} = \mathrm{Re}\left(- \int_\Omega \frac{\partial u_i'}{\partial x_j} \frac{\partial u_i'^*}{\partial x_j} d\Omega \right),$$

$$E_{buoy} = \mathrm{Re}\left(\mathrm{Gr} \int_\Omega T' u_i'^* \delta_{i3} d\Omega \right).$$

E_{shear} represents the production of fluctuating kinetic energy by shear of the basic flow, E_{visc} the viscous dissipation of fluctuating kinetic energy, and E_{buoy} the production of fluctuating kinetic energy by buoyancy. At threshold, the critical eigenvector is associated with an eigenvalue with zero real part. This implies that $\partial K/\partial t$ is equal to zero at marginal stability. Finally, we normalize Eq. (16) by $-E_{visc}=|E_{visc}|$, which is always positive, to get an equation involving normalized energy terms $E'=E/|E_{visc}|$ at threshold:

$$E'_{shear} + E'_{buoy} = 1. \tag{17}$$

The total shear and buoyancy contributions are plotted in Fig. 15, together with the nine components of the shear contribution, for A_y=6 and different values of A_x [Fig. 15(a)] and for A_x=4 and different values of A_y [Fig. 15(b)]. From these figures, it is clear that the dominant production of fluctuating kinetic energy is due to the shear of the basic flow. This term is close to 1 in all cases and thus balances the viscous dissipation term, whereas the buoyancy contribution, slightly stabilizing, remains very weak. A detailed analysis of the different shear contributions clearly indicates that the production of fluctuating kinetic energy by shear of the basic flow is essentially due to the term $[w'(\frac{\partial u}{\partial z})u'^*]$. This term is really dominant with values between 0.9 and 1.5. The term $[w'(\frac{\partial w}{\partial z})w'^*]$ is also destabilizing, but its maximum value, obtained for small A_x, is less than 0.2. The other shear terms are either very weak or stabilizing. The main stabilizing terms $[u'(\frac{\partial u}{\partial x})u'^*]$ and $[u'(\frac{\partial w}{\partial x})w'^*]$ have minimum values which stay above −0.5 and −0.3, respectively.

The above results demonstrate that for all the studied cases covering a wide range of aspect ratios and Prandtl number values, the flow transition is triggered by the shear of the basic flow and primarily by the variation of the basic horizontal velocity with respect to the vertical direction. This

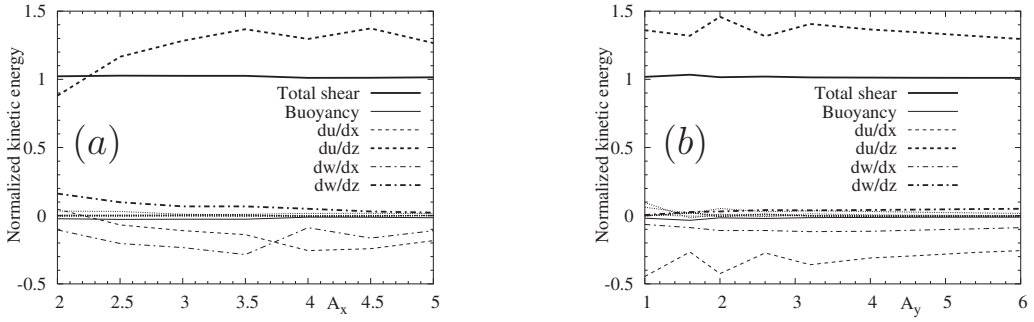

FIG. 15. Fluctuating kinetic energy balance at the critical thresholds: (a) for A_y=6 and different values of A_x and (b) for A_x=4 and different values of A_y (Pr=0.01). The energy contributions have been normalized by the viscous dissipation. Solid lines represent the total production by shear (thick lines) and the buoyancy contribution (thin lines). The different shear contributions are given as dotted lines, except the four largest, those connected to $(\partial u/\partial x)$ and $(\partial u/\partial z)$ given as dashed lines (thin and thick, respectively) and those connected to $(\partial w/\partial x)$ and $(\partial w/\partial z)$ given as long-and-short-dashed lines (thin and thick, respectively).

remains valid despite the large variations of the thresholds and the very frequent change of flow structures at the thresholds. Note that the dominating destabilizing influence of $\left[w'\left(\frac{\partial u}{\partial z}\right)u'^{*}\right]$ was already mentioned in Henry and Buffat [18] and Hof *et al.* [12] for side-heated cavities with aspect ratios $A_x=4$, $A_y=2$ and $A_x=5$, $A_y=1.3$, respectively.

IV. CONCLUSION

Thanks to a performing three-dimensional continuation method allowing an accurate simulation of flows and direct calculation of bifurcation points, we have been able to obtain a kind of map of the transitions for a laterally heated parallelepipedic cavity in a wide range of characteristic parameters. The types of transitions very often change when aspect ratios and Prandtl number are modified; this determines multiple branches of stability thresholds characterized by their steady or oscillatory character and by the symmetries of the critical mode involved.

The transitions generally occur on basic flows involving a roll-like structure inside the long-scale circulation. This structure is the result of an imperfect bifurcation connected to the destabilization of the parallel flow solution in an infinitely extended side-heated cavity.

Concerning the oscillatory transitions, the four types of transitions corresponding to the different possible symmetries in the system have been obtained. In the case where a steady transition occurs first, the oscillatory transition occurs farther on the bifurcated steady branch and is still of another type. Concerning the effect of the Prandtl number, the main result is that the behavior obtained in the limit case Pr=0 is not representative of what occurs in the whole range of weak values of Pr corresponding to liquid metals. Our result is particularly striking as the behavior obtained at Pr=0 is not valid beyond Pr=0.0001.

Finally, it has been shown that the flow transitions arise in all cases because of shear effects and primarily the vertical shear of the longitudinal flow.

ACKNOWLEDGMENT

The calculations were carried out on NEC-SX5 and NEC-SX8 computers with the support of the CNRS through the "Institut du développement et des ressources en informatique scientifique."

[1] G. Müller and A. Ostrogorsky, in *Handbook of Crystal Growth: Growth Mechanisms and Dynamics*, edited by D. T. J. Hurle (North-Holland, Amsterdam, 1993), Vol. 2b.
[2] D. T. J. Hurle, Philos. Mag. **13**, 305 (1966).
[3] D. T. J. Hurle, E. Jakeman, and C. P. Johnson, J. Fluid Mech. **64**, 565 (1974).
[4] J. E. Hart and J. M. Pratte, in *GAMM Workshop: Numerical Simulation of Oscillatory Convection in low-Pr Fluids*, edited by B. Roux, *Notes on Numerical Fluid Mechanics*, Vol. 27 (Vieweg, Braunschweig, 1990), p. 329.
[5] M. C. Hung and C. D. Andereck, Phys. Lett. A **132**, 253 (1988).
[6] J. E. Hart, J. Fluid Mech. **132**, 271 (1983).
[7] J. M. Pratte and J. E. Hart, J. Cryst. Growth **102**, 54 (1990).
[8] M. C. Hung and C. D. Andereck, in *GAMM Workshop: Numerical Simulation of Oscillatory Convection in low-Pr Fluids*, edited by B. Roux, *Notes on Numerical Fluid Mechanics*, Vol. 27 (Vieweg, Braunschweig, 1990), p. 338.
[9] Y. Kamotani and T. Sahraoui, J. Heat Transfer **112**, 253 (1990).
[10] M. G. Braunsfurth and T. Mullin, J. Fluid Mech. **327**, 199 (1996).
[11] A. Juel, T. Mullin, H. BenHadid, and D. Henry, J. Fluid Mech. **436**, 267 (2001).
[12] B. Hof, A. Juel, L. Zhao, D. Henry, H. BenHadid, and T. Mullin, J. Fluid Mech. **515**, 391 (2004).
[13] J. E. Hart, J. Atmos. Sci. **29**, 687 (1972).
[14] P. Laure, J. Mec. Theor. Appl. **6**, 351 (1987).
[15] H. P. Kuo and S. A. Korpela, Phys. Fluids **31**, 33 (1988).
[16] *GAMM Workshop: Numerical Simulation of Oscillatory Convection in low-Pr Fluids*, edited by B. Roux, *Notes on Numerical Fluid Mechanics*, Vol. 27 (Vieweg, Braunschweig, 1990).
[17] M. Afrid and A. Zebib, Phys. Fluids A **2**, 1318 (1990).
[18] D. Henry and M. Buffat, J. Fluid Mech. **374**, 145 (1998).
[19] S. Wakitani, J. Heat Transfer **123**, 77 (2001).
[20] H. BenHadid and D. Henry, J. Fluid Mech. **333**, 57 (1997).
[21] G. E. Karniadakis, M. Israeli, and S. A. Orszag, J. Comput. Phys. **97**, 414 (1991).
[22] C. K. Mamun and L. S. Tuckerman, Phys. Fluids **7**, 80 (1995).
[23] A. Bergeon, D. Henry, H. BenHadid, and L. S. Tuckerman, J. Fluid Mech. **375**, 143 (1998).
[24] G. Petrone, E. Chénier, and G. Lauriat, Int. J. Heat Mass Transfer **47**, 3889 (2004).
[25] T. C. Oppe, W. D. Joubert, and D. R. Kincaid, NSPCG, a package for solving large sparse linear systems by various iterative methods, Center for Numerical Analysis, University of Texas at Austin, 1989.